Performance Projection of a High Temperature CO_2 Transport Membrane Reactor for Combined CO_2 Capture and Methane-to-Ethylene Conversion

Xin Li[1], Kevin Huang[1], Noah Van Dam[2], Xinfang Jin[2*]

[1] Mechanical Engineering Department, University of South Carolina, Columbia, SC29201
[2] Mechanical Engineering Department, University of Massachusetts, Lowell, MA01854
*Corresponding author: Xinfang_Jin@uml.edu

Abstract

Direct conversion of methane into ethylene through the oxidative coupling of methane (OCM) is a technically important reaction. However, conventional co-fed fixed-bed OCM reactors still face serious challenges in conversion and selectivity. In this paper, we apply a finite element model to simulate OCM reaction in a plug-flow CO_2/O_2 transport membrane (CTM) reactor with a directly captured CO_2 and O_2 mixture as a soft oxidizer. The CTM is made of three phases: molten carbonate, 20% Sm-doped CeO_2, and $LiNiO_2$. The membrane parameters are first validated by CO_2/O_2 flux data obtained from CTM experiments. The OCM reaction is then simulated along the length of tubular plug-flow reactors filled with a La_2O_3-CaO-modified CeO_2 catalyst bed, while a mixture of CO_2/O_2 is gradually added through the wall of the tubular membrane. A 12-step OCM kinetic mechanism is considered in the model for the catalyst bed and validated by data obtained from a co-fed fixed-bed reactor. The modeled results indicate a much-improved OCM performance by membrane reactor in terms of C_2-yield and CH_4 conversion rate over the state-of-the-art, co-fed, fixed-bed reactor. The model further reveals that improved performance is fundamentally rooted in the gradual methane conversion with CO_2/O_2 offered by the plug-flow membrane reactor.

Keywords: CO_2 transport membranes, oxidative coupling of methane, membrane reactor, methane conversion rate, C_2 selectivity.

I. Introduction

A recent notable development in the energy field is the significantly increased production of natural gas (NG) from shale and tight oil [1]. If the newly available, low-cost NG is only used for producing heat and power as in the past, it will continue to emit a significant amount of CO_2 into the atmosphere and add burdens to the current effort to mitigate global warming and climate change issues [2, 3]. Alternatively, NG can be directly converted into value-added products with minimal CO_2 emissions [4]. This direct methane conversion (DMC) approach is also economically attractive due to higher economic values of the final products [5, 6].

The most studied DMC technology is Oxidative Coupling of Methane (OCM), transforming CH_4 into ethylene (C_2H_4) with molecular O_2 as the oxidant in a single step [7]. A major technical challenge for the OCM process is to achieve high CH_4 conversion at high C2 selectivity [8]. A number of new reactor designs have been proposed based on the concept of controlling the oxygen content to prevent over-oxidation of the desirable C2 products [9].

From a design perspective, there are generally three types of reactors: moving or fluidized-bed reactor, fixed-bed reactor, and membrane reactor [10, 11]. For the moving or fluidized bed reactors, the solid catalysts need to be replenished at a high frequency in order to remove coke and achieve a C2 yield greater than 50% [12, 13]. However, it is energy intensive to invest in larger reactor vessels, regenerate a large amount of solid catalyst, and provide high pumping power to move the catalyst. For fixed-bed reactors, there is little control over the over-oxidation of C2 such that C2 yield is often limited to <25% [14]. There were some proposed fixed-bed reactors with the ability to control the oxygen concentration in a continuous reactor by distributing the oxygen feed during the reaction to reduce the over-oxidation of C2 products. But, distributing oxygen feed in a reactor is not trivial and could become very costly [15]. The membrane reactors reported in the open literature are either porous membrane reactors or membrane reactors with solid-oxide O_2 transport materials (OTMs) [16, 17]. However, the improvement in C2 yield and selectivity demonstrated so far is still marginal [18].

To control oxygen concentration, previous studies have shown that using nitrogen oxide, carbon dioxide, or sulfur as a soft oxidizer can appreciably improve the conversion-selectivity relationship [19]. Here in this study, we investigate from a modeling perspective the performance of a membrane reactor to directly convert methane to ethylene via OCM using a mixture of CO_2/O_2. In this case, a multi-phase, high-temperature CO_2 transport membrane (CTM) is used to separate CO_2 and O_2 from a carbon source such as flue gas and simultaneously react with methane on the other side of the membrane to form ethylene in the presence of OCM catalysts. We combine experimental data from the most recent CTM study and reaction kinetics of La_2O_3-CaO-modified CeO_2 catalyst in a Multiphysics micromodel to predict CH_4 conversion rate and C2 yield in a new plug-flow membrane reactor. The performance of the reactor is then compared with a fixed-bed reactor counterpart to show the advantages of the new technology.

II. Types of Reactors Simulated

In this study, we simulate a tubular plug-flow membrane reactor and a fixed-bed reactor for model/experiment coupling and comparison purposes. The working principle of each reactor is schematically illustrated in Fig. 1a and 1b. In the membrane reactor (Fig.1c), the CTM consists of three phases: Sm-doped CeO_2 as the solid oxide (SO) phase, molten eutectic Li_2CO_3-Na_2CO_3 as the molten carbonate (MC) phase, and the $LiNiO_2$ (LNO) phase formed in-situ between NiO and MC working as the electron conducting phase [20]. With such a membrane composition, only CO_2 and O_2 in the flue gas can permeate through the membrane to react with methane on the other side.

The central passage of the plug-flow membrane reactor is filled with La_2O_3-CaO-modified CeO_2 catalyst having a 34% porosity. A pure stream of methane is fed into the reactor through the catalyst bed, while a mixture of CO_2, O_2, and N_2 as a mockup of the flue gas from power plants is fed along the outer surface of the reactor. During operation, the CTM gradually adds CO_2 and O_2 into the methane chamber under the gradient of chemical potentials of CO_2 and O_2. There are eleven catalytic reactions (solid line in the reaction network shown in Fig.1d) on the surface and one bulk reaction in the gas phase (dashed line in the same plot) considered inside the reactor (methane chamber). The corresponding reaction kinetics have been listed in Table 1. Ethylene is the product in the outlet. A 2D axial symmetrical model was built to simulate the performance of a membrane reactor coupled with a catalyst bed, shown in Fig.1e. r axis represents the radius direction and z axis is the longitudinal direction of the tubular reactor. The gas species is flowing in the z direction, entering from the left and exiting from the right.

In the fixed-bed reactor (Fig. 1f), the composition, diameter, and length, as well as the porosity of the catalyst bed, and the inlet CH_4 flow velocity are the same as the membrane reactor. There are, however, two major differences in the fixed-bed reactor modeling compared to the membrane reactor: 1) a mixture of CH_4 and CO_2/O_2 is co-fed at the inlet of the reactor; 2) there is only one computational domain for the catalyst bed.

III. Mathematical Models

In this section, we give more details about the mathematical models used to simulate both OCM reactors. The reaction kinetics of OCM on La_2O_3-CaO-modified CeO_2 catalyst involves many species. A 10-step kinetic model was first proposed by Stansch et al. [21] for O_2 OCM. It describes the differential rates of formation of different species under a wide range of operating conditions ($1<p_{O2}<20$kPa, $10<p_{CH4}<95$kPa, $973<T<1228$K). The kinetic model includes thermal cracking, steam reforming and water gas shift reactions, see Table 1. The kinetic parameters are estimated based on experimental data obtained from a microcatalytic fixed bed reactor in the model and experiment coupling section [1]. The reaction rate equations are either in the Hougen-Watson type (reaction 1-6) or the Power-law type (reaction 7-10). In addition, we also considered direct reaction between CH_4 and CO_2 as reaction (11) with the experimental data from Wang et al. [22].

Table 2 lists the governing equations and boundary conditions in both the membrane and the catalyst bed. The model was solved using commercial finite element package Comsol 5.4, Mathematics/The General Form PDE interface. A mapped mesh with 3500 linear quadrilateral elements was used in discretization. According to the definition of our previous work [23], the membrane consists of three phases: molten carbonate phase transporting carbonate ions, mixed oxide and electron conducting phase transporting both oxide-ions and electrons, and the LNO phase transporting electrons only. Therefore, there are four charge conservation equations in the membrane domain. The details of the governing equations and boundary conditions can be found in our previous work [23]. In the catalyst bed, the diffusion and convection of the gas species are described by transport of dilute species in porous media. The reaction kinetics at the catalyst surface or the bulk are given in Table 3. The velocity of the gas stream is assumed to be constant.

To evaluate the overall performance of the OCM reactors, three metrics are used: C2 yield (Y_{C_2}), selectivity (S_{C_2}), and CH_4 conversion rate (C_{CH4}), which are calculated by:

$$Y_{C_2} = S_{C_2} \cdot C_{CH4} \tag{1}$$

$$S_{C_2} = \frac{[2\times(J_{C_2H_4,out}-J_{C_2H_4,in})+2\times(J_{C_2H_6,out}-J_{C_2H_6,in})]}{J_{CH4,in}-J_{CH4,out}} \tag{2}$$

$$C_{CH4} = \frac{J_{CH4,in}-J_{CH4,out}}{J_{CH4,in}} \tag{3}$$

IV. Model and Experiment Coupling

Parameters of the CTM and the catalyst bed were tuned to fit each model separately with each set of experimental data. The 1D CTM model was fitted by experimental data from the button cell of our previous work [23]. Here, we extend the model from 1D [21] to 2D. Therefore, in Fig. 2a, we compare the CO_2 fluxes calculated by both 1D and 2D models with experimental data and found good agreement among the three sets of data. So, we think the membrane parameters extracted from experimental button cell data can be used to simulate the performance of a pilot-scale membrane.

Model and experiment coupling of the O_2 OCM catalyst bed is done by optimization of the C2 yield and CH_4 conversion rate to fit their experimental data obtained from a micro-catalytic fixed-bed reactor with La_2O_3/CaO catalyst as reported by Stansch [24, 25]; the results are shown in Fig. 2b and 2c. With the obtained 10-step reaction kinetic parameters listed in Table 3, an actual micro-catalytic reactor shown in Fig. 1 is simulated. Model and experiment coupling of reaction 11 with CaO/modified CeO_2 catalyst for CO_2 direct oxidation of CH_4 is done with experimental data [22]; the results are shown in Fig. 2d.

After the model and experiment coupling, a composite catalyst La_2O_3/CaO/modified CeO_2 catalyst for both O_2 OCM and CO_2 OCM has been used in the model as the catalyst bed. It is then used to simulate the performance of a membrane reactor and a fixed-bed reactor with the same catalyst bed dimensions and operating conditions given in Table 4. The material properties in the table are obtained from the fitting process.

V. Results and Discussion

In this section, we compare the simulated performance of a membrane reactor and a fixed-bed reactor with the same catalyst bed and operating conditions. The operating temperature is varied between 973K and 1103K. The purpose of this study is to demonstrate the improved performance with the new membrane reactor over the state-of-the-art fixed-bed reactor.

5.1 Fixed-Bed Reactor

Figure 3 shows 2D axial symmetric molar fraction profiles of gas species in a co-fed fixed-bed reactor under 1103K. Note that the 2D domain will be rotated around its vertical orientation to form a cylinder in 3D. CH_4 and CO_2/O_2 streams are co-flowing from the top inlet to the bottom outlet of the cylindrical catalyst bed. To ensure a fair comparison, CO_2/O_2 flowrates are the same as their equivalent flowrates permeated through the membrane in the membrane reactor. The wall of the container is under zero-flux boundary condition. It can be seen that CH_4 and CO_2/O_2 have been continuously converted to CO, C_2H_6, C_2H_4, H_2O and H_2, as the stream move toward the outlet (bottom) of the tubular reactor.

To show the gas species molar fraction profiles along the flow direction under different temperatures quantitatively, we plotted their profiles along the z-axis of the cylindrical catalyst bed, see Fig. 4. Since CH_4 molar fraction is much higher than the rest of the species, it is not plotted here. CH_4 conversion rate will be discussed in section 5.3. The inlet corresponds to z=0mm and outlet is at z=400mm. The following trends are observed: 1) The molar fraction of C_2H_6 increases with temperature from 973K to 1023K, and then decreases sharply toward 1103K. 2) The produced molar fraction of C_2H_4 surpassed that for C_2H_6 at 1103K. 3) The molar fraction of H_2O rises sharply first and then stays flat around 0.09 as temperature increases. 4) CO molar fraction is below 0.02 for all three cases. 5) O_2 molar fraction decreases fast with temperature and then becomes depleted at 1103K. 6) CO_2 molar fraction profiles are quite stable for the lower temperatures but started to decrease largely at 1103K.

To understand the molar fraction profiles of all species and its relationship with the catalytic and bulk reactions in the fixed-bed reactor, the reaction rates of all 11 reactions listed in Table 1 are plotted along the z-axis of the reactor. There are 10 catalytic reactions (1-6, 8-11) with a unit of mol/kg/s, and 1 bulk reaction (7) with a unit of $mol/m^3/s$. The catalytic reactions are plotted against the left y-axis in Fig. 5 and the bulk reaction is plotted against the right y axis. Reaction 3 (producing undesirable C1), and reaction2 2 and 11 (producing desirable C2) are the most significant reactions. Reaction 3 shows a decreasing trend along the z axis and decreases faster at higher temperatures. The bulk reaction 7 converts C_2H_6 to C_2H_4 and its reaction rate is enhanced by higher temperatures. Its profile in the z axis direction is correlated to the reactant C_2H_6 molar fraction. Even though reactions 2 and 11 (C2 reaction) and reaction 7 (from C_2H_6 to C_2H_4) have been significantly enhanced at 1103K, reactions 5 (convert C_2H_6 to C_2H_4) and 6 (convert C_2H_4 to CO) have also been facilitated, which prevents further increase of C2 product in Fig. 4.

5.2 Membrane Reactor

Different from the fixed-bed reactor, in the membrane reactor, pure CH_4 is fed at the inlet, while CO_2/O_2 is gradually added into the reactor through the CTM. The catalyst bed of the membrane reactor is the same as that for the fixed-bed reactor. The CH_4 inflow velocity is the same as that for the fixed-bed reactor. The flux of CO_2/O_2 is determined by the in-situ CO_2/O_2 partial pressure gradients across the membrane and varies along the z-axis. Their overall flux is the same as that at the inlet of the fixed bed reactor.

Figure 6 shows 2D axial symmetric gas species molar fraction profiles along the membrane reactor at 1103K, from which we can see that: 1) CO_2 and O_2 are gradually added into the reactor through the wall of the membrane reactor. 2) CH_4 is consumed in the bulk of the reactor and there is a significant variation along the radial direction since there are more abundant O_2 and CO_2 permeated from the membrane at the inner surface. 3) Both C2 products (C_2H_6 and C_2H_4) are produced in the bulk of the reactor, and their molar fraction are slightly higher along the membrane inner surface. 4) Large amounts of H_2O and H_2 are also produced at the outlet of the reactor. 5) CO molar fraction is the lowest in the reactor.

Figure 7 shows the molar fraction variations along the membrane inner surface in the z-axis direction. Compared to their counterparts' plots for fixed-bed reactors, there are three major differences: 1) C2 (C_2H_4 and C_2H_6) molar fractions are higher for the membrane reactor, especially at higher temperature 1103K. 2) H_2O product mole fraction is twice as high compared with that for the fixed-bed reactor. 3) CO_2 molar fraction becomes dominant species in the product stream, indicating higher CH_4 oxidation rate. As temperature increases, CO_2 domination has been weakened by H_2O.

Figure 8 further confirms the enhanced reaction kinetics for more desirable reactions, such as reactions 2 and 11 (producing C_2H_6), and reaction 5 (producing C_2H_4), especially towards the outlet of the reactor. Therefore, elongating the reactor in the flow direction could further improve its performance by enhancing CO_2/O_2 OCM reaction.

5.3 Performance Comparison

To compare the overall performance of the two different OCM reactors, C2 yield and selectivity, as well as CH_4 conversion rate from Eq. 1-3 are plotted against operating temperature in Fig. 9. One can see that 1) for the fixed bed reactor, C2 yield reaches the maximum of ~15% around 1023K, whereas for the membrane reactor, it continues to increase as the temperature increases; 2) C2 selectivity for the membrane reactor remains above 93% while that for the fixed-bed falls under 91% at 1103K; 3) The CH_4 conversion rate for the membrane reactor is more than twice that of the fixed-bed reactor at 1103K. At the same time, a significant amount of CO_2 has been captured in the membrane reactor from the flue gas.

In Fig. 10a, CO_2/O_2 flux along the membrane inner surface in the z-axis direction is plotted. It increases with temperature but decreases exponentially along the z-axis from the inlet to the outlet at a given temperature. At the inlet, large amount of CO_2/O_2 is needed to convert CH_4 to C2 products; as the stream approaches the outlet, CO_2/O_2 concentration in the membrane reactor increases, which reduces the driving force for the chemical potential driven diffusion process and leads to reduced CO_2/O_2 flux. In Fig. 10b, CH_4 molar fraction is plotted against the z-axis. It decreases along the z-axis from the inlet to the outlet. The CH_4 molar fraction decreases more abruptly along the z axis in the membrane reactor than that in the fixed-bed reactor, which is consistent with the CH_4 conversion rate shown in Fig. 9c.

The comparison results in Fig.9 and Fig. 10 indicate that the membrane reactor shows improved performance under higher temperatures in terms of C2 yield/selectivity and CH_4 conversion rate. However, in practical operation a lower operating temperature is preferred to maintain a longer lifetime of the reactor. An alternative solution to improve the reactor performance at lower temperatures is to lengthen the reactors. The fixed-bed reactor has a well-known limitation in C2 yield. As shown in Fig. 11, C2 yield is plateaued at 20% with a reactor length higher than 1.4 m. But for the membrane reactor, as the length increases, C2 yield linearly increases and could reach as high as 32% with a reactor length of 2 m. Therefore, it is economically beneficial to run a longer membrane reactor for combined CO_2 capture and OCM under lower temperatures.

5.4 Coking resistance

Coke formation during OCM reaction is thermodynamically and kinetically favorable, particularly under controlled oxygen conditions to avoid over-oxidation, leading to loss of catalyst's activity via pore blockage, collapse of the catalyst support, or physical blockage of the tube in the fixed-bed reactor [30]. Coking is a major challenge for OCM to be commercially viable. The coking possibility of OCM in fixed-bed and membrane reactors is assessed by analyzing thermodynamic equilibrium with the gas composition calculated at the outlet of the reactors from the Comsol models under different temperatures. The results are shown in Fig. 12. Coking selectivity is defined as the moles of carbon produced divided by the moles of CH_4 consumed. From the figure, we find that: 1) For the fixed bed reactor, coking selectivity decreases by more than 50% as temperature increases from 970K to 1120K, which is caused by fast reaction kinetics and abundance of CO_2/H_2O in the gas stream. 2) For the membrane reactor, a similar trend is observed but coking selectivity is slightly higher under low temperatures and much lower under high temperatures. Such improved coking resistance is due to the superior CH_4 conversion rate of the membrane reactor under high temperatures. Therefore, we conclude that a higher operating temperature is beneficial to suppress coke formation. Along the gas flow direction, more oxidizers such as CO_2 and O_2 will be continually added into the reactor through the membrane, which will reduce coking.

5.5 Direct CO_2 oxidative coupling of methane

For the results presented in sections 5.1-5.3, direct oxidation of methane by CO_2 (reaction 11) has been included. Compared to O_2-OCM (reaction 2), CO_2-OCM is more challenging given the nature of the stable CO_2 molecule. However, using CO_2 as an oxidizer for OCM has implications to mitigating CO_2 emissions. In recent years, explorative studies on direct CO_2-OCM have been reported [30, 31], but with very low C2 yields (3 - 6% depending on CO_2 partial pressure in the gas mixture). In this study, we use the experimental data produced from CaO-modified CeO_2

catalyst [32] to obtain the reaction kinetics parameter for reaction 11 in Table 3 and then incorporate the reaction into the models for fixed-bed reactor and membrane reactor. Referring to the C2 yield for OCM with O_2 in Figure 11, Figure 13 shows that the maximum C2 yield increase vs. temperature of direct CH_4 oxidation by CO_2, which is similar for fixed-bed and membrane reactors, 2.5% for the fixed-bed reactor vs. 2% for the membrane reactor at the highest temperature 1120K and a reactor length of 0.4 m. For longer reactors, there will be more residence time for CO_2 to react with CH_4. However, it is evident that CO_2-OCM contribution is marginal compared to O_2-OCM, regardless of the type of reactor. New catalysts would be needed to boost CO_2-OCM. As of now, the ability to capture CO_2 and incremental addition of O_2 into CH_4 stream for OCM are the major advantages for the membrane reactors.

VI. Conclusion

In summary, we have developed a membrane reactor model to simulate the performance of a combined CO_2 capture and CH_4 oxidative coupling reaction. The model parameters are obtained by validating experimental data of C2 yield and CH_4 conversion rate from a microcatalytic fixed-bed reactors, as well as CO_2 flux in a lab-scale membrane. The results show that the membrane reactor has the following advantages over its counterpart fixed-bed reactor design. 1) The membrane reactor can overcome C2 yield limitation faced by the fixed bed reactor under higher operating temperatures or longer reactor length and achieve over 30% C2 yield. 2) CO_2 molar fraction becomes dominant in the membrane reactor product stream, indicating a higher CH_4 conversion rate. 3) Longer membrane reactor shows better coking resistance compared to its fixed-bed counterpart design. 4) Direct oxidation of CH_4 by CO_2 could only improve the C2 yield in the membrane reactor by 2%, suggesting that OCM is mainly carried out by O_2. We show that the membrane reactor with high intrinsic CO_2 flux can become an efficient bifunctional device for simultaneous CO_2 capture and CH_4-to-C_2H_4 conversion through OCM reaction. Further technoeconomic analysis will be conducted to assess the commercialization potential of the technology in the future.

Acknowledgments

This material is based upon work supported by the U.S. National Science Foundation under grant number CBET-1924095.

NOMENCLATURE

Symbols	Unit	Physical Meaning
c	mol/m^3	Molar fraction
D	m^2/s	Diffusion coefficient
Ea	J/mol	Activation energy in the reaction step j
F		Faraday's constant
ΔH	J/mol	Enthalpy
J	A/cm^2	Current
k		Pre-exponential factor
K	Pa^{-1}	Adsorption constant
m, n		Reaction order
N	mol/m^2/s	Molar Flux
P	Pa	Partial pressure
R	J/(mol·K)	Gas constant
T	K	Temperature
Z		Charge
Greek Symbols		
ε		Volume fraction of molten carbonate
σ	S/m	Conductivity
Φ	V	Electric potential
μ	J/mol	Chemical potential
τ		Tortuosity
Subscripts and superscripts		
ad		adsorption
C		Carbonate ion
D		Cation defect
e		Electron in metal phase
n		Electron in solid oxide phase
MC		Molten carbonate phase
LNO		$LiNiO_2$ phase
V		Oxide vacancy

References

1. Li-Chiang Lin, Adam H. Berger, Richard L. Martin, Jihan Kim, Joseph A. Swisher, Kuldeep Jariwala, Chris H. Rycroft, Abhoyjit S. Bhown, Michael W. Deem, Maciej Haranczyk and Berend Smit, *In silico screening of carbon-capture materials.* Nat Mater, 2012. **11**(7): p. 633-41.
2. Raymond T. Pierrehumbert, *High levels of atmospheric carbon dioxide necessary for the termination of global glaciation.* Nature, 2004. **429**(6992): p. 646-9.
3. Hans R. Schultz, *Climate change and viticulture: A European perspective on climatology, carbon dioxide and UV-B effects.* Australian Journal of Grape and Wine Research, 2000. **6**(1): p. 2-12.
4. Peng Zhang, Jingjing Tong, Kevin Huang, Xuefeng Zhu, Weishen Yang, *The current status of high temperature electrochemistry-based CO2 transport membranes and reactors for direct CO2 capture and conversion.* Progress in Energy and Combustion Science, 2021. **82**.
5. Peng Zhang, Jingjing Tong, and Kevin Huang, *Self-Formed, Mixed-Conducting, Triple-Phase Membrane for Efficient CO2/O2 Capture from Flue Gas and in Situ Dry-Oxy Methane Reforming.* ACS Sustainable Chemistry & Engineering, 2018. **6**(11): p. 14162-14169.
6. Peng Zhang, Jingjing Tong, and Kevin Huang, *A Study of Low-Cost NiO-MC Dual-Phase Membrane for High-Flux and Selective Electrochemistry-Based CO2Capture.* ECS Transactions, 2017. **80**(10): p. 861-870.
7. Jack H. Lunsford, *The Catalytic Oxidative Coupling of Methane.* Angewandte Chemie International Edition in English, 1995. **34**(9): p. 970-980.
8. D. Schweer, L. Meeczko, and M. Baerns, *OCM in a fixed-bed reactor: limits and perspectives.* Catalysis Today, 1994. **21**(2-3): p. 357-369.
9. Stanislav Jaso, Hamid Reza Godini, Harvey Arellano-Garcia, and Gunter Wozny, *Oxidative Coupling of Methane: Reactor Performance and Operating Conditions.* Computer Aided Chemical Engineering, 2010. **28**: p. 6.
10. Worapon Kiatkittipong, Tomohiko Tagawa, Shigeo Goto, Suttichai Assabumrungrat, Kampol Silpasup, and Piyasan Praserthdam, *Comparative study of oxidative coupling of methane modeling in various types of reactor.* Chemical Engineering Journal, 2005. **115**(1-2): p. 63-71.
11. A. Cruellas, T. Melchiori, F. Gallucci, and M. van Sint Annaland, *Advanced reactor concepts for oxidative coupling of methane.* Catalysis Reviews, 2018. **59**(3): p. 234-294.
12. Anna Lee Tonkovich, Robert W. Carr, and Rutherford Aris, *Enhanced c2 yields from methane oxidative coupling by means of a separative chemical reactor.* Science, 1993. **262**(5131): p. 221-3.
13. S. Jašo, S. Sadjadi, H.R. Godini, U. Simon, S, Arndt, O. Gorke, A. Berthold, H. Arellano-Garcia, H. Schubert, R. Schomacker, and G. Wozny, *Experimental investigation of fluidized-bed reactor performance for oxidative coupling of methane.* Journal of Natural Gas Chemistry, 2012. **21**(5): p. 534-543.
14. Nakisa Yaghobi, and Mir Hamid Reza Ghoreishy, *Oxidative coupling of methane in a fixed bed reactor over perovskite catalyst: A simulation study using experimental kinetic model.* Journal of Natural Gas Chemistry, 2008. **17**(1): p. 8-16.

15. F.M. Dautzenberg, J.C. Schlatter, J.M. Fox, J.R. Rostrup-Nielsen, L.J. Christiansen, *Catalyst and reactor requirements for the oxidative coupling of methane.* Catalysis Today, 1992. **13**(4): p. 503-509.
16. Subhash Bhatia, Chua Yen Thien, and Abdul Rahman Mohamed, *Oxidative coupling of methane (OCM) in a catalytic membrane reactor and comparison of its performance with other catalytic reactors.* Chemical Engineering Journal, 2009. **148**(2-3): p. 525-532.
17. W. Wang, and Y.S. Lin, *Analysis of oxidative coupling of methane in dense oxide membrane reactors.* Journal of Membrane Science, 1995. **103**(3): p. 219-233.
18. Y. K. Kao, L. Lei, and Y.S. Lin, *A Comparative Simulation Study on Oxidative Coupling of Methane in Fixed-Bed and Membrane Reactors.* Industrial & Engineering Chemistry Research, 1997. **36**(9): p. 3583-3593.
19. Allison M. Arinaga, Morgan C. Ziegelski, and Tobin J. Marks, *Alternative Oxidants for the Catalytic Oxidative Coupling of Methane.* Angew Chem Int Ed Engl, 2021. **60**(19): p. 10502-10515.
20. Peng Zhang, Jingjing Tong, and Kevin Huang, *A self-forming dual-phase membrane for high-temperature electrochemical CO2 capture.* Journal of Materials Chemistry A, 2017. **5**(25): p. 12769-12773.
21. Z. Stansch, L. Mleczko, and M. Baerns, *Comprehensive Kinetics of Oxidative Coupling of Methane over the La2O3/CaO Catalyst.* Industrial & Engineering Chemistry Research, 1997. **36**(7): p. 2568-2579.
22. Wang, Y., Y. Takahashi, and Y. Ohtsuka, *Carbon Dioxide as Oxidant for the Conversion of Methane to Ethane and Ethylene Using Modified CeO2 Catalysts.* Journal of Catalysis, 1999. **186**(1): p. 160-168.
23. Xin Li., Kevin Huang, and Xinfang Jin, *Mathematical Modeling of High-Temperature Multiphase Solid/Molten Carbonate Membranes for CO2 Capture.* Journal of The Electrochemical Society, 2020. **167**(16): p. 164512.
24. Z. Stansch., *Kinetics for oxidative coupling of methane process over La2O3/CaO catalyst.* 1995, Ruhr-University Bochum, Bochum.
25. Ching Thian Tye, Abdul Rahman Mohamed, and Subhash Bhatia, *Modeling of catalytic reactor for oxidative coupling of methane using La2O3/CaO catalyst.* Chemical Engineering Journal, 2002. **87**(1): p. 49-59.
26. ToolBox, E. *Air - Diffusion Coefficients of Gases in Excess of Air.* 2018; Available from: https://www.engineeringtoolbox.com/air-diffusion-coefficient-gas-mixture-temperature-d_2010.html.
27. T. Kojima, Y. Miyazaki, K. Nomura, and K. Tanimoto, *Physical Properties of Molten Li2CO3-Na2CO3(52:48 mol%) and Li2CO3-K2CO3(62:38 mol%) Containing Additives.* Journal of The Electrochemical Society, 2013. **160**(10): p. H733-H741.
28. A. Atkinson, *Chemically-induced stresses in gadolinium-doped ceria solid oxide fuel cell electrolytes.* Solid State Ionics, 1997. **95**(3): p. 249-258.
29. Shaorong Wang, Takehisa Kobayashi, Masayuki Dokiya, and Takuya Hashimoto, *Electrical and Ionic Conductivity of Gd-Doped Ceria.* Journal of The Electrochemical Society, 2000. **147**(10): p. 3606.
30. Jason M. Ginsburg, Juliana Pina, Tarek El Solh, and Hugo I. de Lasa, *Coke Formation over a Nickel Catalyst under Methane Dry Reforming Conditions: Thermodynamic and Kinetic Models.* Industrial & Engineering Chemistry Research, 2005. **44**(14): p. 4846-4854.

31. Xiaojiao Cai, and Yun Hang Hu, *Advances in catalytic conversion of methane and carbon dioxide to highly valuable products.* Energy Science & Engineering, 2019. **7**(1): p. 4-29.
32. Yongzheng Zhang, Yohei Cho, Akira Yamaguchi, Xiaobo Peng, Masahiro Miyauchi, Hideki Abe, and Takeshi Fujita, *CO2 oxidative coupling of methane using an earth-abundant CaO-based catalyst.* Sci Rep, 2019. **9**(1): p. 15454.

Tables

Table 1 Reactions and Kinetic Rates [21]

Index	Reaction	Reaction Kinetics
1	$CH_4 + 2O_2 \rightarrow CO_2 + 2H_2O$	$r_1 = \frac{\left(k_{01}\cdot e^{-\frac{E_a}{RT}}\right)\cdot P_{CH4}^{m_1}\cdot P_{O_2}^{n_1} - k_b v e^{-\frac{E_a}{RT}}\cdot P_{CO_2}^{m_1}\cdot P_{H_2O}^{n_1}}{(1+K_{1,CO_2}\cdot e^{-\frac{\Delta H_{ad,CO_{2},1}}{RT}}\cdot P_{CO_2})^2}$
2	$2CH_4 + 0.5O_2 \rightarrow C_2H_6 + H_2O$	$r_2 = \frac{k_{02}\cdot e^{-\frac{E_a}{RT}}\cdot(K_{0O_2}\cdot e^{-\frac{\Delta H_{adO_2}}{RT}}P_{O_2})^{n_2}P_{CH_4}}{[1+\left(K_{0,O_2}\cdot e^{-\frac{\Delta H_{ad,O_2}}{RT}}\cdot P_{O_2}\right)^{n} + K_{2,CO_2}\cdot e^{-\frac{\Delta H_{ad,O_2}}{RT}}P_{O_2}]^2}$
3	$CH_4 + O_2 \rightarrow CO + H_2O + H_2$	$r_3 = \frac{\left(k_{03}\cdot e^{-\frac{E_a}{RT}}\right)\cdot P_{CH4}^{m_3}\cdot P_{O_2}^{n3} - k_b\cdot e^{-\frac{E_a}{RT}}\cdot P_{CO_2}^{m_3}\cdot P_{H_2O}^{n_3}}{(1+K_{3,CO_2}\cdot e^{-\frac{\Delta H_{ad,CO_{2},3}}{RT}}\cdot P_{CO_2})^2}$
4	$CO + 0.5O_2 \rightarrow CO_2$	$r_4 = \frac{\left(k_{04}\cdot e^{-\frac{E_a}{RT}}\right)\cdot P_{CH4}^{m_4}\cdot P_{O_2}^{n4} - k_b\cdot e^{-\frac{E_a}{RT}}\cdot P_{CO_2}^{m_4}\cdot P_{H_2O}^{n_4}}{(1+K_{4,CO_2}\cdot e^{-\frac{\Delta H_{ad,CO_{2},4}}{RT}}\cdot P_{CO_2})^2}$
5	$C_2H_6 + 0.5O_2 \rightarrow C_2H_4 + H_2O$	$r_5 = \frac{\left(k_{05}\cdot e^{-\frac{E_a}{RT}}\right)\cdot P_{CH4}^{m_5}\cdot P_{O_2}^{n5} - k_b\cdot e^{-\frac{E_a}{RT}}\cdot P_{CO_2}^{m_5}\cdot P_{H_2O}^{n_5}}{(1+K_{5,CO_2}\cdot e^{-\frac{\Delta H_{ad,CO_{2},5}}{RT}}\cdot P_{CO_2})^2}$
6	$C_2H_4 + 2O_2 \rightarrow 2CO + 2H_2O$	$r_6 = \frac{\left(k_{06}\cdot e^{-\frac{E_a}{RT}}\right)\cdot P_{CH4}^{m_6}\cdot P_{O_2}^{n6} - k_b\cdot e^{-\frac{E_a}{RT}}\cdot P_{CO_2}^{m_6}\cdot P_{H_2O}^{n_6}}{(1+K_{6,CO_2}\cdot e^{-\frac{\Delta H_{ad,CO_{2},6}}{RT}}\cdot P_{CO_2})^2}$
7	$C_2H_6 \rightarrow C_2H_4 + H_2$	$r_7 = k_{07}\cdot e^{-\frac{E_{a7}}{RT}}P_{C_2H_6}$
8	$C_2H_4 + 2H_2O \rightarrow 2CO + 4H_2$	$r_8 = k_{08}\cdot e^{-\frac{E_{a8}}{RT}}P_{C_2H_4}^{m_8}\cdot P_{H_2O}^{n_8}$
9	$CO + H_2O \rightarrow CO_2 + H_2$	$r_9 = k_{09}\cdot e^{-\frac{E_{a9}}{RT}}P_{CO}^{m_9}P_{H_2O}^{n_9}$
10	$CO_2 + H_2 \rightarrow CO + H_2O$	$r_{10} = k_{10}\cdot e^{-\frac{E_{a10}}{RT}}P_{CO_2}^{m_{10}}P_{H_2}^{n_{10}}$
11	$2CH_4 + CO_2 \rightarrow C_2H_6 + H_2O + CO$	$r_{11} = k_{11}\cdot e^{-\frac{E_{a11}}{RT}}P_{CH_4}^{m_{11}}P_{CO_2}^{n11}$

Table 2 Governing equations and boundary conditions (B. C.) for different domains

Physics	**Governing Eq.**	**B.C. @ Feed Side (Outer surface)**	**B.C. @ Sweep Side (Inner surface)**
Membrane			
Oxygen vacancy conservation in SO phase	$\nabla \cdot J_V = -\frac{(1-\varepsilon)}{\tau_{SO}}\left(Z_V F D_V \nabla^2 C_V + \frac{{Z_V}^2 F^2 D_V C_V}{RT} \nabla^2 \emptyset_{SO}\right) = 0$	$\emptyset_{SO,0} = \frac{RT\left(\ln\frac{P_{CO_2,0}}{P^0}\frac{C^0}{C_V}\right)-\beta}{FZ_V}$	$J_V + J_n + J_C + J_{n,LNO} = 0$
Molten carbonate ion conservation in MC phase	$\nabla \cdot J_C = -\frac{\varepsilon}{\tau_{MC}} \sigma_C \nabla^2 \emptyset_{MC} = 0$	$\emptyset_{MC}(x = 0) = 0$	$\emptyset_{MC,L} = \frac{RT\left(\ln\frac{P_{CO_2,L}}{P^0}\frac{C^0}{C_V}\right)-\beta}{FZ_C} - \frac{Z_V \emptyset_{SO,L}}{Z_C}$
Electron/hole conservation in SO phase	$\nabla \cdot J_n = -\frac{(1-\varepsilon)}{\tau_{SO}}\left(Z_n F D_n \nabla^2 C_n + \frac{Z_n^2 F^2 D_n C_n}{RT} \nabla^2 \emptyset_{SO}\right) = 0$	$C_n(0) = K_T^{1/2} C_v^{1/2} {P_{O_2,0}}^{1/2}$ $Z_V C_V + Z_n C_n + Z_D C_D = 0$	$C_n(L) = K_T^{1/2} C_v^{1/2} P_{O_2,L}^{1/2}$ $Z_V C_V + Z_n C_n + Z_D C_D = 0$
Electron conservation in metal phase	$\nabla \cdot J_{e,LNO} = -V_{LNO}\left(\sigma_{e,LNO} \nabla^2 \emptyset_{LNO}\right) = 0$	$\emptyset_{LNO,0} = \frac{\chi}{2Z_e F} - \frac{RT}{2Z_e F} \ln \frac{P_{CO_2,0}}{P^0} (\frac{P_{O_2,0}}{P^0})^{0.5}$	$\emptyset_{LNO,L} = \frac{\chi}{2Z_e F} - \frac{RT}{2Z_e F} \ln \frac{P_{CO_2,L}}{P^0} \left(\frac{P_{O_2,L}}{P^0}\right)^{0.5} + \frac{Z_C}{2Z_e} \emptyset_{MC,L}$
Catalyst Bed			
Transport of diluted species in porous media	$\nabla \cdot N_i + \mathbf{u} \cdot \nabla c_i = R_i$ $N_i = -D_i \nabla C_i$	Inflow (Left inlet): $c_i = c_{0,i}$	Outflow (Right outlet): $\mathbf{n} \cdot D_i \nabla c_i = 0$

Table 3 Kinetic Parameters for Catalytic and Bulk Reactions [21]

Index	**k_{0j} $mol^{-1}\times g^{-1}\times s^{-1}\times Pa^{-(m+n)}$**	**$E_{a,j}$**	**$K_{j,CO2}$**	**$\Delta H_{ad,CO2}$,kJ/mol**	**K_{O2},Pa^{-1}**	**$\Delta H_{ad,O2}$**	**m_j**	**n_j**
1	0.2×10^{-5}	48	0.25×10^{-12}	-175	—	—	0.24	0.76
2	23.2	182	0.83×10^{-13}	-186	0.23×10^{-11}	-124	1	0.4
3	0.52×10-^{6}	68	0.36×10^{-13}	-187	—	—	0.57	0.85
4	0.11×10^{-3}	104	0.4×10^{-12}	-168	—	—	1	0.55
5	0.17	157	0.45×10^{-12}	-166	—	—	0.95	0.37
6	0.06	166	0.16×10^{-12}	-211	—	—	1	0.96
7	1.2×10^{7}	226	—	—	—	—	—	—
8	9.3×10^{3}	300	—	—	—	—	0.97	0
9	0.19×10^{-3}	173	—	—	—	—	1.0	1.0
10	0.26×10^{-1}	220	—	—	—	—	1.0	1.0
11	1.8×10^{-7}	140					2	0.5

Table 4 Parameters and Operating Conditions for Both Fixed-Bed and Membrane Reactors

Parameter	Value	Reference
Common Parameters for Both Reactors		
Reactor length	0.4 [m]	[25]
Reactor diameter	0.018 [m]	
Operating temperature	973-1103 [K]	
Sweep gas composition	99.3% CH_4	
CH_4 stream velocity	0.39 [m/s]	
CO_2 diffusivity	1.39×10^{-4}[m^2/s]	[26]
CO diffusivity	1.45×10^{-4}[m^2/s]	
O_2 diffusivity	1.52×10^{-4}[m^2/s]	
CH_4 diffusivity	1.57×10^{-4}[m^2/s]	
C_2H_6 diffusivity	1.31×10^{-4}[m^2/s]	
C_2H_4 diffusivity	1.37×10^{-4}[m^2/s]	
H_2O diffusivity	1.95×10^{-4}[m^2/s]	
H_2 diffusivity	6.20×10^{-4}[m^2/s]	
Membrane Reactor Specific Parameters		
Membrane thickness	0.2 [mm]	[5]
Feed gas composition	15% CO_2: 10% O_2:75% N_2	[5]
Sweep gas composition	99.3% CH_4	—
LNO conductivity	$\ln\sigma = 5.8456 - \frac{463.9}{T}$ [S/m]	[5]
Molten Carbonate conductivity	$\sigma = -4.6866 + 8.533\cdot10^{-3}\cdot T - 1.325\cdot10^{-6}\cdot T^2$	[27]
SDC20 ionic conductivity	$\sigma_i = \frac{Z_i^2 F^2 D_i C_i}{RT} = Z_i^2 F \mu_i C_i$ $\log_{10}\left(\mu_{i,10}T\right) = 2.4656 - 3.40416\cdot\frac{1000}{T}$ $\log_{10}\left(\mu_{i,20}T\right) = 2.36515 - 3.56931\cdot\frac{1000}{T}$	[28, 29]
SDC20 electronic conductivity	$\log_{10}\left(\mu_{e,10}T\right) = 4.1943 - 4.30072\cdot\frac{1000}{T}$ $\log_{10}\left(\mu_{e,20}T\right) = 2.63204 - 2.6264\cdot\frac{1000}{T}$	[28, 29]
Tortuosity of the solid oxide phase	2.5	[23]
Tortuosity of the molten carbonate phase	$\ln\tau_{MC} = -9.2167 + \frac{11234.4}{T}$	[23]
Tortuosity of the LNO phase	$\tau_{LNO} = 0.5768 + 0.0055\cdot T$	[23]
Volume fraction of molten carbonate	0.5	[23]
Volume fraction of LNO phase	0.01	[23]
Fixed-Bed Reactor Specific Parameters		
Inlet gas composition	8.7%CO_2, 4.3%O_2, 87% CH_4	[25]

Figure Captions

Figure 1 Schematic Illustration of (a) Membrane reactor; (b) Co-fed fixed bed reactor. (c) charge species transport and surface reactions in the membrane reactor. (d) Reaction pathway diagram. (Numbers correspond to reaction indexes given in Table 1). 2D axial symmetric computational domain of (e) Membrane reactor; (f) Co-fed fixed bed reactor.

Figure 2 (a) CO_2 flux of the membrane. O_2 OCM for the fixed catalyst bed: (b) C2 yield; (c) CH_4 conversion rate, blue curve is from [25]. (d) CO_2 OCM for the fixed catalyst bed, experimental data is from [22].

Figure 3 2D axial symmetric gas species molar fraction profiles in the fixed-bed reactor under 1103K. (Gas is flowing from the top inlet to the bottom outlet.)

Figure 4 Molar fractions of gas species in the co-fed fixed-bed reactor along the z axis under (a) 973K; (b) 1023K; (c) 1103K.

Figure 5 Reaction rates in the fixed-bed reactor along the z axis under(a) 973K; (b) 1023K;(c) 1103K

Figure 6 2D axial symmetric gas species molar fraction profiles in the membrane reactor under 1103K. (Gas is flowing from the top inlet to the bottom outlet.)

Figure 7 Molar fractions of gas species in the membrane reactor along the z axis under (a) 973K; (b) 1023K; (c) 1103K.

Figure 8 Reaction rates in the membrane reactor along the z axis under(a) 973K; (b) 1023K; (c) 1103K

Figure 9 Performance comparison between membrane and fixed-bed reactors: (a) C2 yield; (b) C2 selectivity; (c) CH_4 conversion rate.

Figure 10 (a) CO_2 flux along the gas/membrane interface in the membrane reactor; (b) CH_4 molar fraction comparison between membrane and fixed-bed reactors.

Figure 11 C2 Yield as a function of reactor length.

Figure 12 Coking Selectivity as a function of operating temperature.

Figure 13 C2 yield increase for membrane reactor and fixed-bed reactor considering the OCM by CO_2.

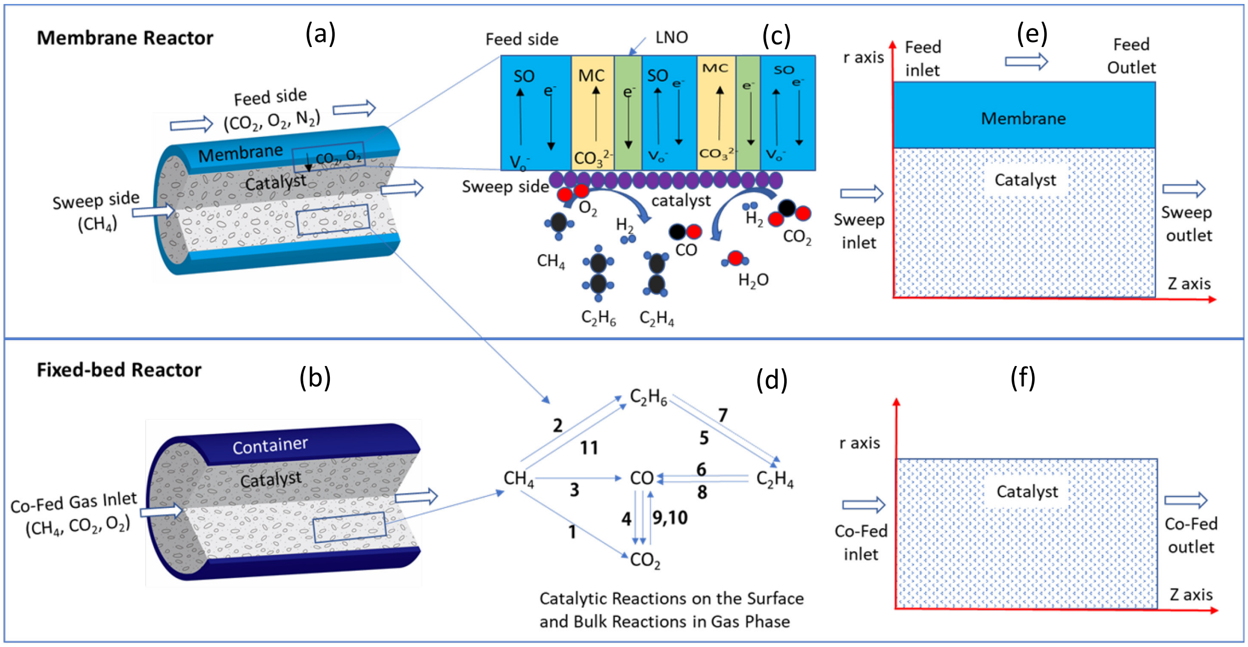

Figure 1 Schematic Illustration of (a) Membrane reactor; (b) Co-fed fixed bed reactor. (c) charge species transport and surface reactions in the membrane reactor. (d) Reaction pathway diagram. (Numbers correspond to reaction indexes given in Table 1). 2D axial symmetric computational domain of (e) Membrane reactor; (f) Co-fed fixed bed reactor.

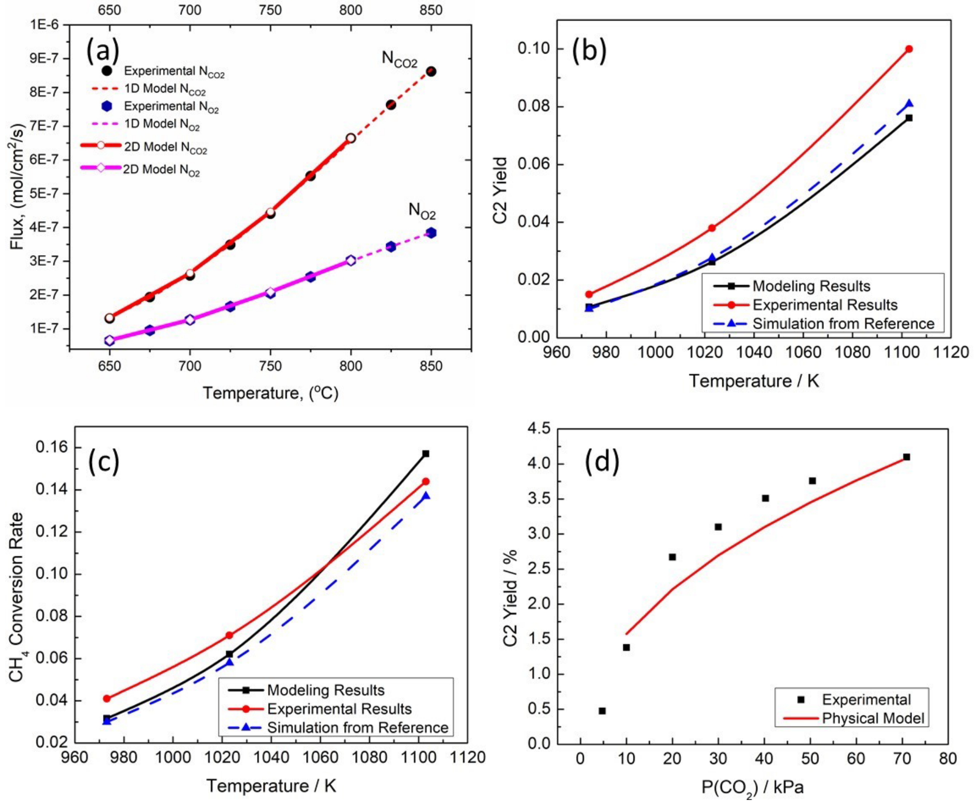

Figure 2 (a) CO_2 flux of the membrane. O_2 OCM for the fixed catalyst bed: (b) C2 yield; (c) CH_4 conversion rate, blue curve is from [25]. (d) CO_2 OCM for the fixed catalyst bed, experimental data is from [22].

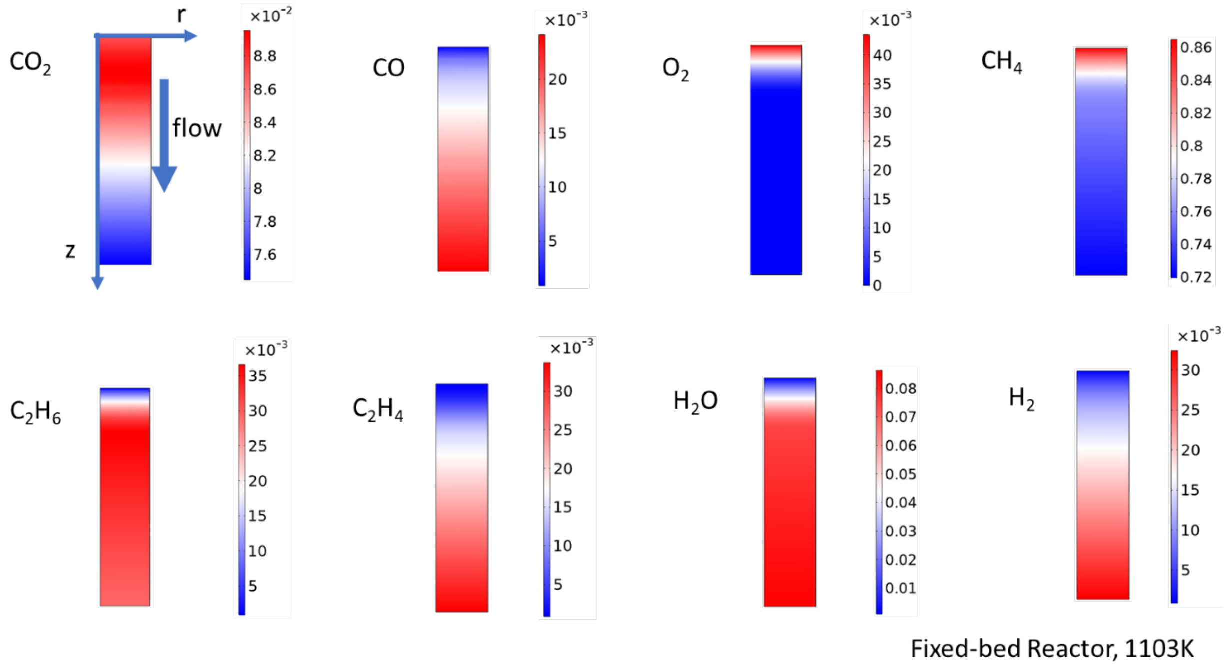

Figure 3 2D axial symmetric gas species molar fraction profiles in the fixed-bed reactor under 1103K. (Gas is flowing from the top inlet to the bottom outlet.)

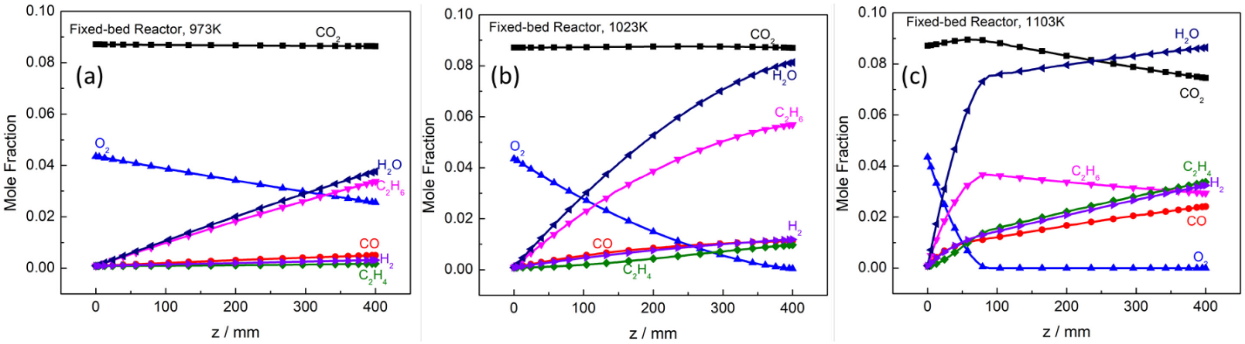

Figure 4 Molar fractions of gas species in the co-fed fixed-bed reactor along the z axis under (a) 973K; (b) 1023K; (c) 1103K.

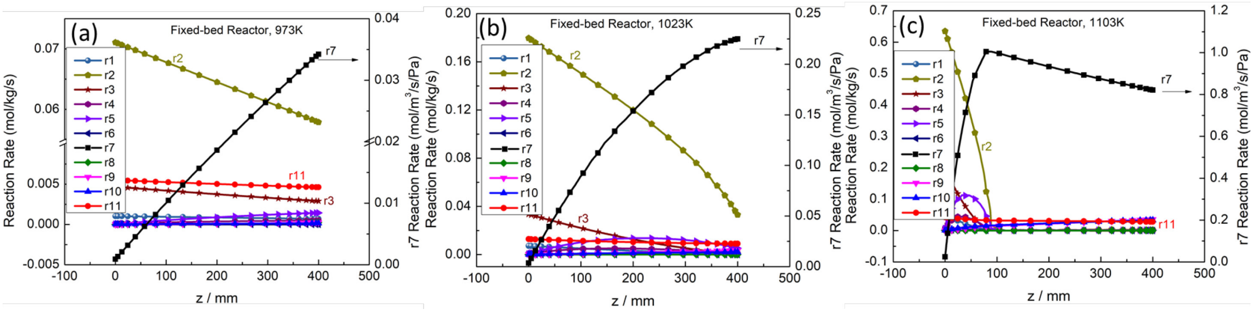

Figure 5 Reaction rates in the fixed-bed reactor along the z axis under(a) 973K; (b) 1023K;(c) 1103K

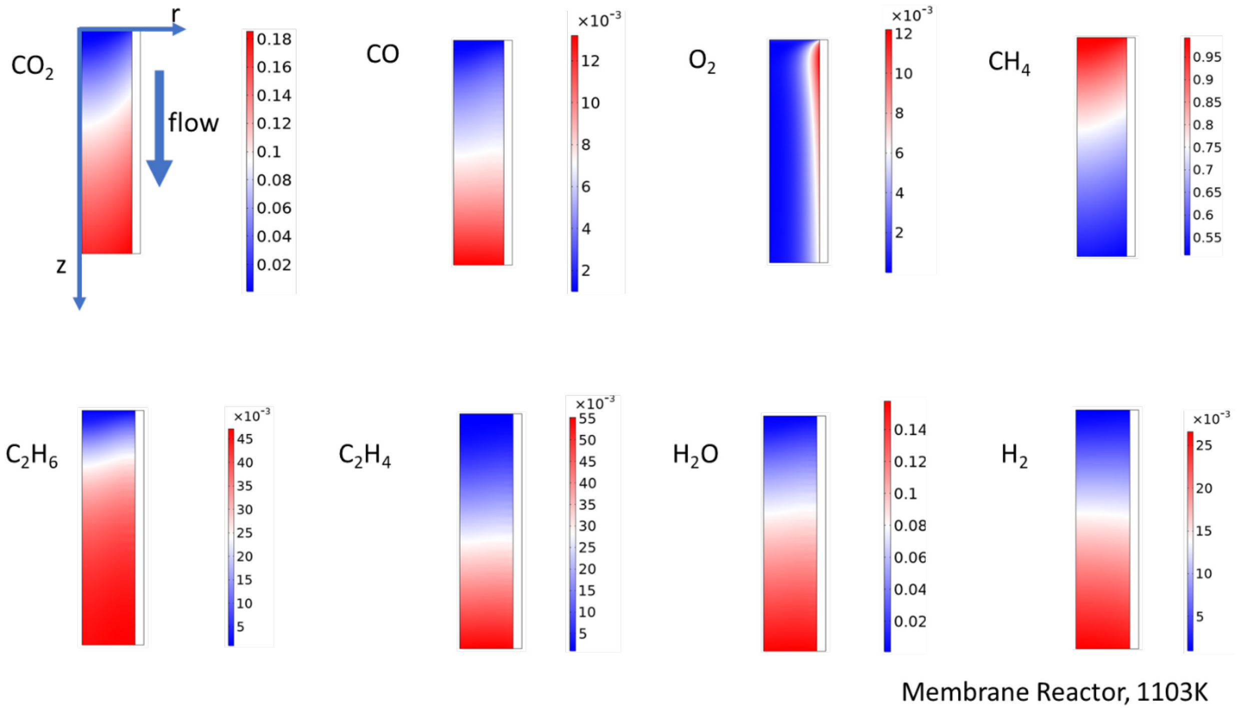

Figure 6 2D axial symmetric gas species molar fraction profiles in the membrane reactor under 1103K. (Gas is flowing from the top inlet to the bottom outlet.)

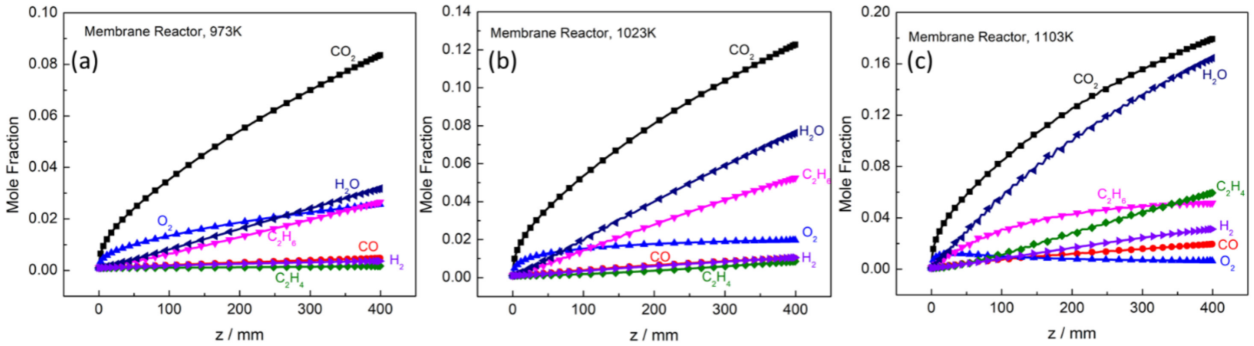

Figure 7 Molar fractions of gas species in the membrane reactor along the z axis under (a) 973K; (b) 1023K; (c) 1103K.

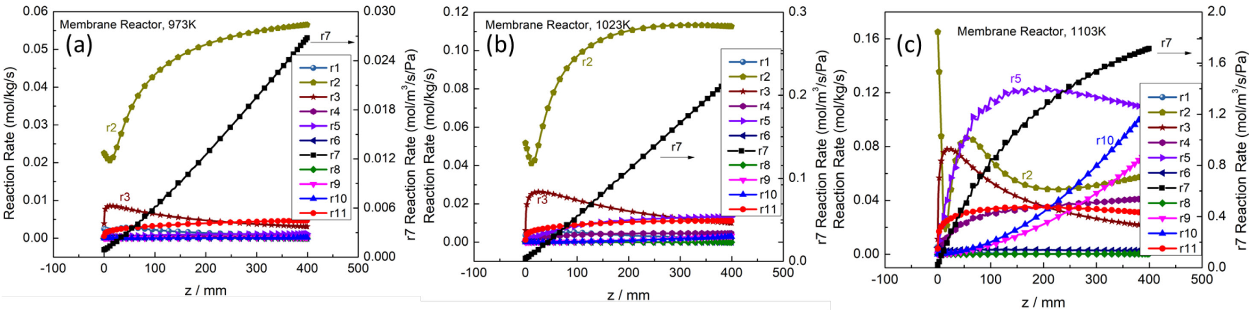

Figure 8 Reaction rates in the membrane reactor along the z axis under(a) 973K; (b) 1023K; (c) 1103K

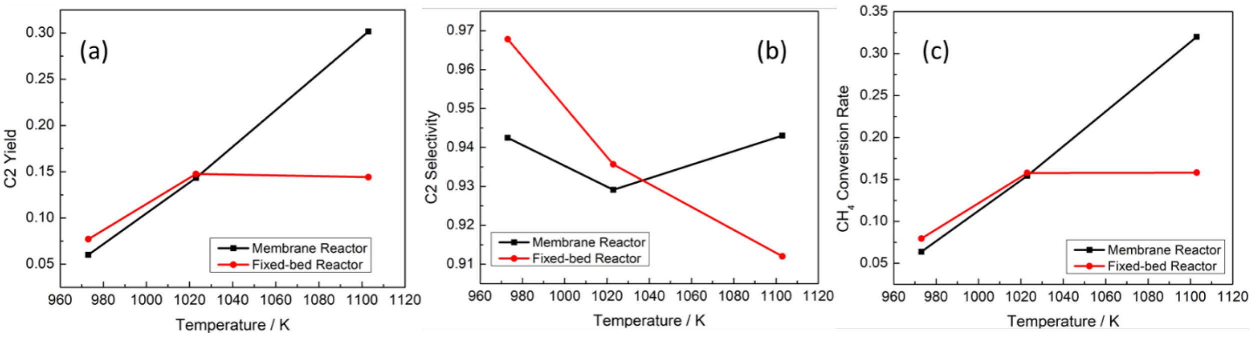

Figure 9 Performance comparison between membrane and fixed-bed reactors: (a) C2 yield; (b) C2 selectivity; (c) CH_4 conversion rate.

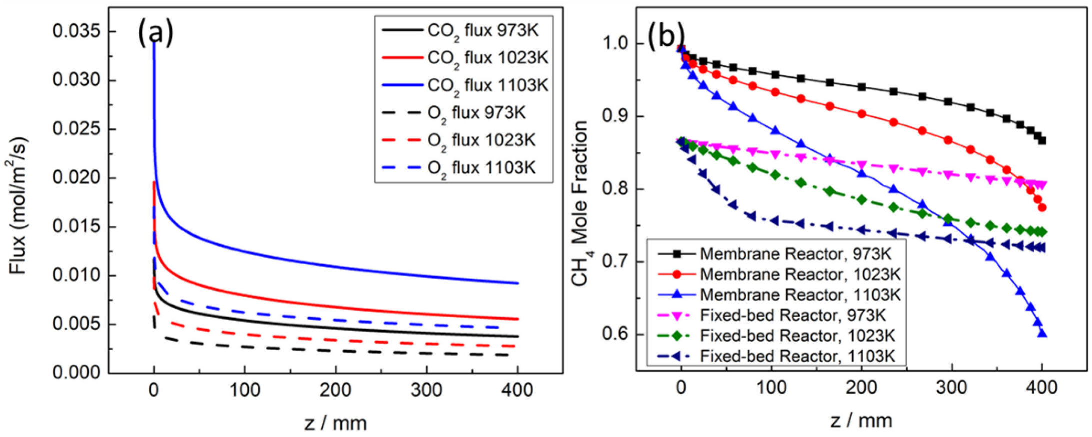

Figure 10 (a) CO_2 flux along the gas/membrane interface in the membrane reactor; (b) CH_4 molar fraction comparison between membrane and fixed-bed reactors.

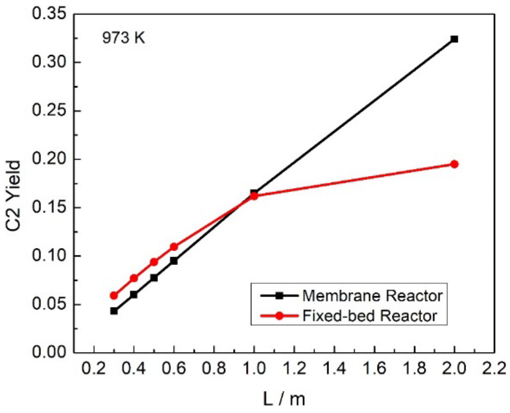

Figure 11 C2 Yield as a function of reactor length.

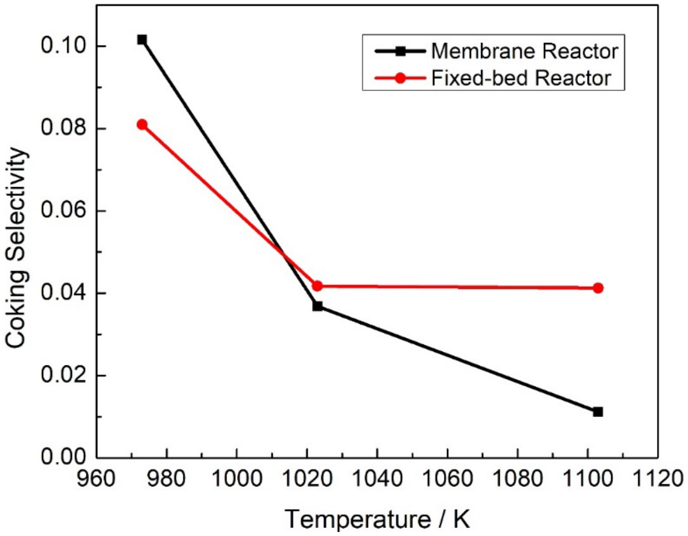

Figure 12 Coking Selectivity as a function of operating temperature.

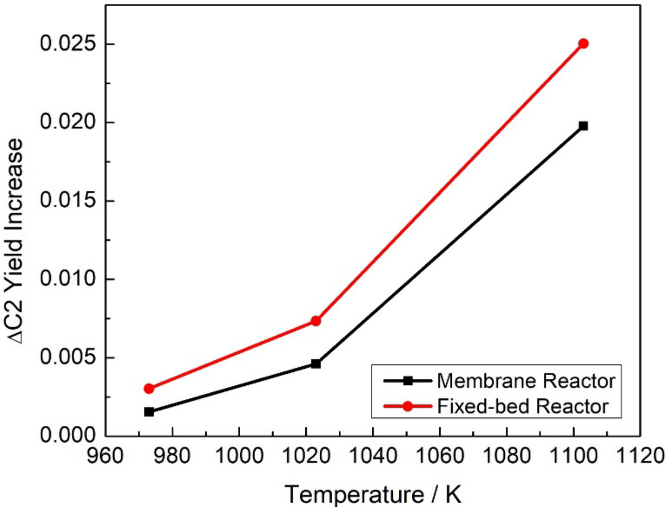

Figure 13 C2 yield increase for membrane reactor and fixed-bed reactor considering the OCM by CO_2.